(This is a sample cover image for this issue. The actual cover is not yet available at this time.)

Applied Catalysis B: Environmental 136–137 (2013) 122–132

Contents lists available at SciVerse ScienceDirect

Applied Catalysis B: Environmental

journal homepage: www.elsevier.com/locate/apcatb

Reduction and catalytic behaviour of nanostructured Pd/gadolinia-doped ceria catalysts for methane combustion

Fernando F. Muñoz [a], Richard T. Baker [b], A. Gabriela Leyva [c,d], Rodolfo O. Fuentes [c,*]

[a] CINSO (Centro de Investigaciones en Sólidos), CONICET-CITEDEF, J.B. de La Salle 4397, 1603 Villa Martelli, Buenos Aires, Argentina
[b] EaStChem, School of Chemistry, University of St. Andrews, North Haugh, St. Andrews, Fife, KY16 9ST, United Kingdom
[c] Departamento de Física, Centro Atómico Constituyentes, CNEA, Av. Gral. Paz 1499, (1650) San Martín, Buenos Aires, Argentina
[d] Escuela de Ciencia y Tecnología, Universidad Nacional de San Martín, Av. Gral. Paz 1499, (1650) San Martín, Buenos Aires, Argentina

ARTICLE INFO

Article history:
Received 29 November 2012
Received in revised form 28 January 2013
Accepted 2 February 2013
Available online xxx

Keywords:
Solid oxide fuel cells
Supported Pd catalysts
Nanostructured ceria-gadolinia catalyst supports
HRTEM
X-ray powder diffraction
X-ray absorption spectroscopy

ABSTRACT

In the present work, 1 wt% and 5 wt% Pd/GDC10 ($Gd_{0.1}Ce_{0.9}O_{1.95}$) nanopowders were prepared by two different methods: (a) cation complexation (CC) and (b) incipient wetness impregnation (WI) of an aqueous Pd^{2+} solution onto GDC10 nanopowders. All samples were characterised by X-ray diffraction (XRD), thermal analysis (TG/DTA), specific surface area determination and high resolution transmission electron microscopy (HRTEM). In order to study the oxidation state of Pd in samples with and without reducing treatments, XANES experiments at the Pd L_3-edge were carried out. In situ Ce L_3-edge XANES experiments were performed under reducing conditions in order to investigate the reduction behaviour of these materials. The addition of Pd to the GDC10 nanopowders increased the reducibility of Ce in the mixed oxide. Finally, catalytic tests for CH_4 combustion were performed on the Pd/GDC10 nanopowders. Catalysts with higher Pd loading (5 wt%) exhibited the best performance for CH_4 combustion. The influence of preparation method was evident for catalysts with 1 wt% Pd, the cation complexation method resulting in more active catalysts than the wetness impregnation method.

1. Introduction

Rare earth-doped ceria (CeO_2) powders have a number of important applications, such as in three-way catalysts and solid oxide fuel cell (SOFC) devices [1–6]. A vast range of catalytic applications make use of the reversible oxygen storage ability of ceria-based materials, a phenomenon which is closely connected to the Ce^{4+}/Ce^{3+} redox couple [7]. For similar reasons, it would be advantageous to use GDC in anode materials in intermediate temperature (IT)-SOFCs. Several studies in this area have been reported, especially on the use of GDC as a catalyst support [8–10]. For this application in particular, it is necessary to obtain materials with large specific surface area (SSA). This has prompted a renewed interest in the preparation of these materials in the form of nanosized powders or shape-controlled nanostructures [11,12].

Hydrocarbons are proposed as fuels for SOFCs. Among the hydrocarbons, methane (CH_4), being the main component of natural gas, is of particular importance. Direct, electrochemical conversion of methane in a fuel cell would represent a significant improvement in efficiency, and so a dramatic reduction in CO_2 production, over conventional methane combustion for electricity generation [13–16].

Nanostructured ceria materials can be used as supports for highly dispersed noble metal nanoparticles. The resulting catalyst systems exhibit much improved catalytic activity and redox properties. The most widely used material for this purpose is CeO_2–ZrO_2 because these compositions can undergo fast and reversible redox reactions. Such materials are also under investigation for application as SOFC anodes by the authors [17–19]. Several investigators have reported on the noble metal–ceria interaction and its effects on catalytic activity. In particular, Pd-based catalysts are active for NO reduction and CO and hydrocarbon oxidation reactions. The presence of Pd in the crystal lattice of ceria-based catalysts for methane combustion has been reported to show a beneficial catalytic effect [20]. Substitution of Pd^{2+} ions for Ce^{4+} in nano-CeO_2 particles can lead to the highest possible dispersion for a given loading of Pd and to higher chemical and structural stability of the Pd^{2+} ions because of the stabilising effect of the oxygen ions in the CeO_2 lattice [21].

Recently, the authors reported on the synthesis of nanostructured 1 wt% Pd/Gd_2O_3-CeO_2 mixed oxide tubes with 90 mol% CeO_2 [22]. The incorporation of the Pd appeared to destabilise Ce^{4+} towards reduction to Ce^{3+} and so cause a significant increase in the reducibility of the nanotube material.

* Corresponding author. Tel.: +54 1148381602.
E-mail address: rofuentes@conicet.gov.ar (R.O. Fuentes).

0926-3373/$ – see front matter © 2013 Elsevier B.V. All rights reserved.
http://dx.doi.org/10.1016/j.apcatb.2013.02.008

In the present work, 1 wt% and 5 wt% Pd/GDC10 nanopowders were prepared by two different methods: (a) cation complexation (CC) and (b) incipient wetness impregnation (WI) of an aqueous Pd^{2+} solution onto GDC10 nanopowders. All samples were characterised by X-ray diffraction (XRD), thermal analysis (TG/DTA), SSA determination (by the Brunauer–Emmett–Teller (BET) method) and high resolution transmission electron microscopy (HRTEM). In order to study the oxidation state of Pd in samples before and after reducing treatments, X-ray absorption near edge spectroscopy (XANES) experiments at the Pd L_3-edge were carried out. In situ Ce L_3-edge XANES experiments were performed under reducing conditions in order to investigate the reduction behaviour of these materials. Finally, catalytic tests for CH_4 combustion were performed on Pd/GDC10 nanopowders.

2. Experimental

2.1. Preparation of Pd/gadolinia-doped ceria catalysts

Two different methods were employed to obtain nanostructured 1 and 5 wt% $Pd/Gd_{0.1}Ce_{0.9}O_{1.95}$ (GDC10) catalyst: (a) CC and (b) incipient WI of an aqueous solution of $Pd(NO_3)_2$ onto GDC10 nanopowders.

2.1.1. Cation complexation method (CC)

$Ce(NO_3)_3{\cdot}6H_2O$ (99.99%, Alfa Aesar), $Gd(NO_3)_3{\cdot}6H_2O$ (99.9%, Acros) and $Pd(NO_3)_2{\cdot}2H_2O$ (Merck) were employed as precursors. Each nitrate was dissolved in pure H_2O separately and then the solutions were mixed to obtain a nitrate solution with a molar Ce:Gd:Pd stoichiometry appropriate for the preparation of 1 wt% and 5 wt% Pd/GDC10. Citric acid (99.5%, Merck) was dissolved in d.i. water and this was added to the solution of nitrates. The molar ratio of total oxide (TO) to citric acid (CA) was 1:2. A schematic flowchart of the cation complexation method is exhibited in Supporting Data (Fig. S1). The resulting ash-like catalysts were calcined at 600 °C for 1 h in air.

2.1.2. Incipient wetness impregnation (WI)

The GDC10 nanopowder was synthesised by the cation complexation route [23,24]. Catalysts with nominal Pd loadings of 1 wt% and 5 wt% were prepared by incipient wetness impregnation of an aqueous solution of $Pd(NO_3)_2$ onto this GDC10 nanopowder. All resulting catalysts were dried at 100 °C and calcined at 600 °C for 1 h in air, in order to decompose any unreacted nitrate precursor.

2.2. Physico-chemical characterisation

2.2.1. Thermal analysis

Thermal analysis (TG/DTA) of the gel precursors of GDC10 and the 1 wt% and 5 wt% Pd/GDC10 catalysts prepared by the cation complexation route was carried out in flowing air with a heating rate of 10 °C/min up to 800 °C in an Al_2O_3 crucible, using a Shimadzu DTG-50 apparatus.

2.2.2. Electron microscopy

TEM images of the Pd/GDC10 samples were obtained using a JEOL 2010 TEM instrument. This was equipped with a LaB_6 filament and a Gatan digital camera and was operated at 200 keV. The microscope also benefited from a system for performing energy dispersive X-ray spectroscopy (EDS). EDS was used to obtain spectra containing elemental composition data from selected points and areas on the samples. EDS maps were also obtained from 5 to 8 regions of each of the four catalyst materials. In each case, a TEM image and distribution maps for Ce, Gd, O and Pd were obtained.

2.2.3. X-ray diffraction

XRD experiments were carried out using a Philips PW 1710 diffractometer (Cu-Kα radiation). Data in the angular region of $2\theta = 20–100^\circ$ were collected at room temperature in a step-scanning mode, with a step length of 0.04° and a step-counting time of 12 s. Si powder (NIST SRM 640c) was used as the standard for the instrumental broadening correction. The average crystallite size, D_{XRD}, was determined using the Scherrer formula [25], at the peak position of the main reflection (1 1 1). Errors in crystallite size were derived by estimating the error in the FWHM (full-width at half-maximum) to be equal to the 2θ step.

XRD patterns were recorded at high temperatures (HT) and in controlled atmospheres using synchrotron radiation at the D10B-XPD beamline of the National Synchrotron Light Laboratory (LNLS, Campinas, Brazil). In these HT-XRD experiments, the sample was mounted on a ceramic sample-holder and placed in a furnace. In order to detect the rather weak Pd and PdO reflections, a high-intensity low resolution configuration, without crystal analyzer, was employed. The wavelength was set at 1.54892 Å. Data in the angular region $2\theta = 31–44^\circ$ were collected in a step-scanning mode, with a step length of 0.04° and a step-counting time of 2 s. The data were collected at temperatures ranging from room temperature to 500 °C. The sample was heated at a rate of 10 °C/min, and a soak time of 10 min was employed at each temperature step before the scan. The thermal behaviour of the materials was studied in 5% H_2/He (total flow: 20 ml min^{-1}) and in dry synthetic air (total flow: 50 ml min^{-1}).

2.2.4. Nitrogen adsorption–desorption measurements

SSA measurements were carried out using BET absorption isotherm analysis by nitrogen adsorption–desorption (Autosorb-1, Quantachrome). The analysis of the isotherms provided values of the SSA. Outgassing was carried out at 300 °C for 4 h.

2.2.5. X-ray absorption

In order to carry out XANES experiments at the Pd L_3-edge, measurements of soft X-rays were performed at the D04A-SXS beamline of the LNLS. The powdered samples were placed on a carbon tape. X-ray absorption spectra were recorded in fluorescence mode ($E/\Delta E = 5000$). Experiments were performed under vacuum (10^{-8} mbar) at room temperature. The energy scale was calibrated by setting the Pd L_3-edge, defined by the first inflection point of the X-ray absorption spectrum of a Pd metallic foil, to be 3173.4 eV.

In order to determine qualitatively the oxidation state of Ce in the 1 wt% and 5 wt% Pd/GDC10 catalysts, XANES spectra were collected at the D04B-XAFS1 beamline at LNLS in transmission mode using a Si(1 1 1) monochromator for the Ce L_3-edge. The nominal photon flux of the beamline was 3×10^9 photons/(s mrad 100 mA)@6 keV. All spectra were collected at room temperature for energies in the range 5690–5780 eV using steps of 2 eV for 5690–5710 eV and 0.2 eV for 5710–5780 eV, with $E/\Delta E = 5000–10{,}000$. Energy was calibrated using a Cr foil. Several acquisitions (around 4 spectra) were carried out on the same sample to improve the signal to noise ratio.

In situ XANES experiments under conditions of controlled temperature and atmosphere were carried out for Ce using the same parameters and at the same beamline as above. Samples were diluted with boron nitride and these mixtures were pressed into 15 mm diameter pellets (around 6 mg of sample and 70 mg of diluent were used). For the transmission measurements, the pellets were placed in a tubular quartz furnace (diameter, 20 mm; X-ray path length, 440 mm) sealed with refrigerated Kapton windows. Temperature was measured and controlled by a thermocouple passed down the sample holder and positioned close to the surface of the pellet. Temperature-resolved XANES spectra at the Ce L_3-edge were acquired during temperature programmed reduction

(TPR) under 5% H_2/He (total flow: 20 ml min^{-1}) at temperatures from 25 to 600 °C at a heating rate of 10 °C min^{-1} and with a total data acquisition time of 8 min per spectrum. The data were normalised using the programme WinXAS [26].

2.2.6. Catalytic tests for CH_4 combustion

Catalytic studies on 1 wt% and 5 wt% Pd/GDC10 catalysts prepared by CC and WI were performed in a fixed-bed flow reactor (quartz tube of 4 mm internal diameter, 60 cm length), operated isothermally at atmospheric pressure. The reactor was placed in an electric tubular oven equipped with a temperature controller. A thermocouple was placed axially along the quartz tube and directly into the sample as a way to provide an accurate temperature measurement. The sample (45 mg) was diluted with ground quartz wool in order to ensure an adequate contact with the reactants. The reactants were a mixture of methane (1.4 cm^3 min^{-1}) and air (38.5 cm^3 min^{-1}), with nitrogen added to the mixture to provide a total gas flow of 50 cm^3 min^{-1}. In order to determine the extent of non-catalytic combustion of CH_4 in the reactor a blank run was performed using a fixed bed composed of only 400 mg of SiO_2. Measurements were performed in the 200–900 °C temperature range, at 50 °C increments. Several measurements were taken at each temperature until the system reached steady state. Gas analysis was performed using a PerkinElmer Clarus 500 gas chromatograph equipped with a thermal conductivity detector, an Altech CTR1 packed column, and using He as the carrier gas. Moisture was removed from the gases using a desiccant trap prior to injection into the chromatograph.

3. Results and discussion

3.1. Physico-chemical characterisation

Fig. 1 shows the TG/DTA plot (carried out in air) on the gel precursors of the GDC10 and 1 wt% and 5 wt% Pd/GDC10 prepared by the CC method. The DTA curve for pure GDC10 exhibits one exothermic peak, starting at 212 °C, whereas the Pd/GDC10 samples exhibit two exothermic peaks, starting at 93 °C and 250 °C, for both samples. The first one can be ascribed to NO_x release (associated with Pd). The second exothermic peak can be related to the burn out of organic materials, by liberation of NO_x, CO, CO_2, and to the crystallisation of the GDC10 solid solution [24].

From the TG curve it is possible to identify two steps. The total weight loss up to 200 °C was 20% for 1 wt% and 5 wt% Pd/GDC10 whereas for pure GDC10 the total weight loss was about 9%. From 200 °C up to 400 °C, the total weight loss was very similar for all samples (about 50% of the mass at 200 °C). No significant weight loss from 400 °C up to 800 °C was observed (less than 1%).

Samples of the as-prepared 5 wt% Pd catalysts prepared by both the CC and WI methods were studied by HRTEM. A comparison of the structure of these two materials is given in Fig. 2 over a range of magnifications. Both samples were made up of primary particles of around 10–30 nm in diameter. These particles were seen to form sheet-like structures of largely interlocking particles in the CC sample while the WI sample appeared to consist of more three-dimensional structures. The highest resolution images show the internal crystal planes of typical primary particles, and these confirmed the crystalline nature of the products made using both preparation methods. Digital diffraction patterns (DDPs) obtained from the lattice images in Fig. 2c and f gave patterns which could be indexed to the expected cubic Fluorite structure of GDC10 as viewed along the [0 1 1] zone axis (giving **a** ~5.4 Å). Discrete Pd particles could be identified in the 5 wt% Pd/GDC10-CC sample, in Fig. 3a, by measuring the interplanar spacings from the particle shown, and in Fig. 3b, for which a complete DDP is obtained. This

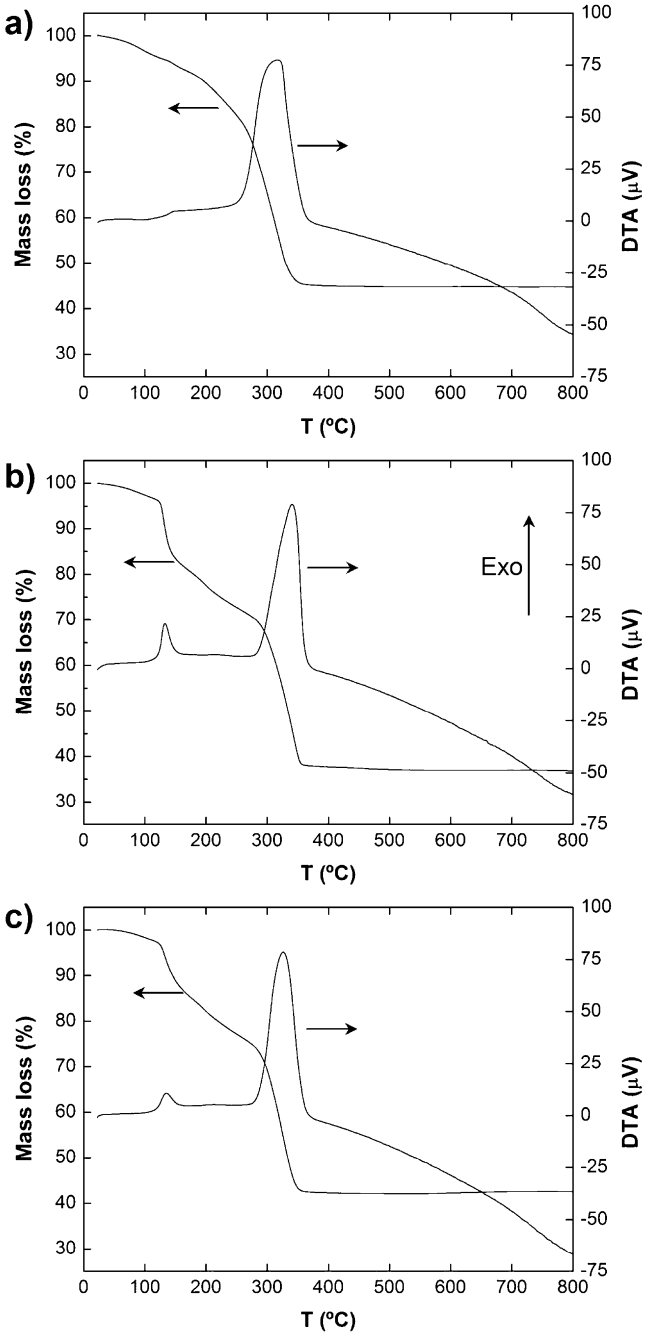

Fig. 1. TG/DTA of metal nitrate precursor mixtures for (a) GDC10, (b) 1 wt% Pd/GDC10 and (c) 5 wt% Pd/GDC10, each obtained by the cation complexation method.

DDP could be indexed to the *fcc* structure of Pd viewed along the [0 1 1] zone axis (giving **a** ~3.8 Å). The Pd particle diameters are around 5–7 nm in these images. Quite similar results were obtained for the 5 wt% Pd/GDC10-WI sample and these are given in Fig. 3c and d. The particle seen in frontal orientation in Fig. 3c was identified from the complete DDP obtained to be Pd viewed along the [0 1 1] zone axis (with **a** ~3.8 Å). The group of particles in Fig. 3d were also identified as Pd both by EDS analysis and from the various interplanar spacings viewed in the overlapping diffraction patterns in the DDP obtained from the image. The Pd particles observed in this sample had diameters of about 4–6 nm.

The observation in these as-prepared samples of metallic Pd crystallites, rather than PdO crystallites as would be expected

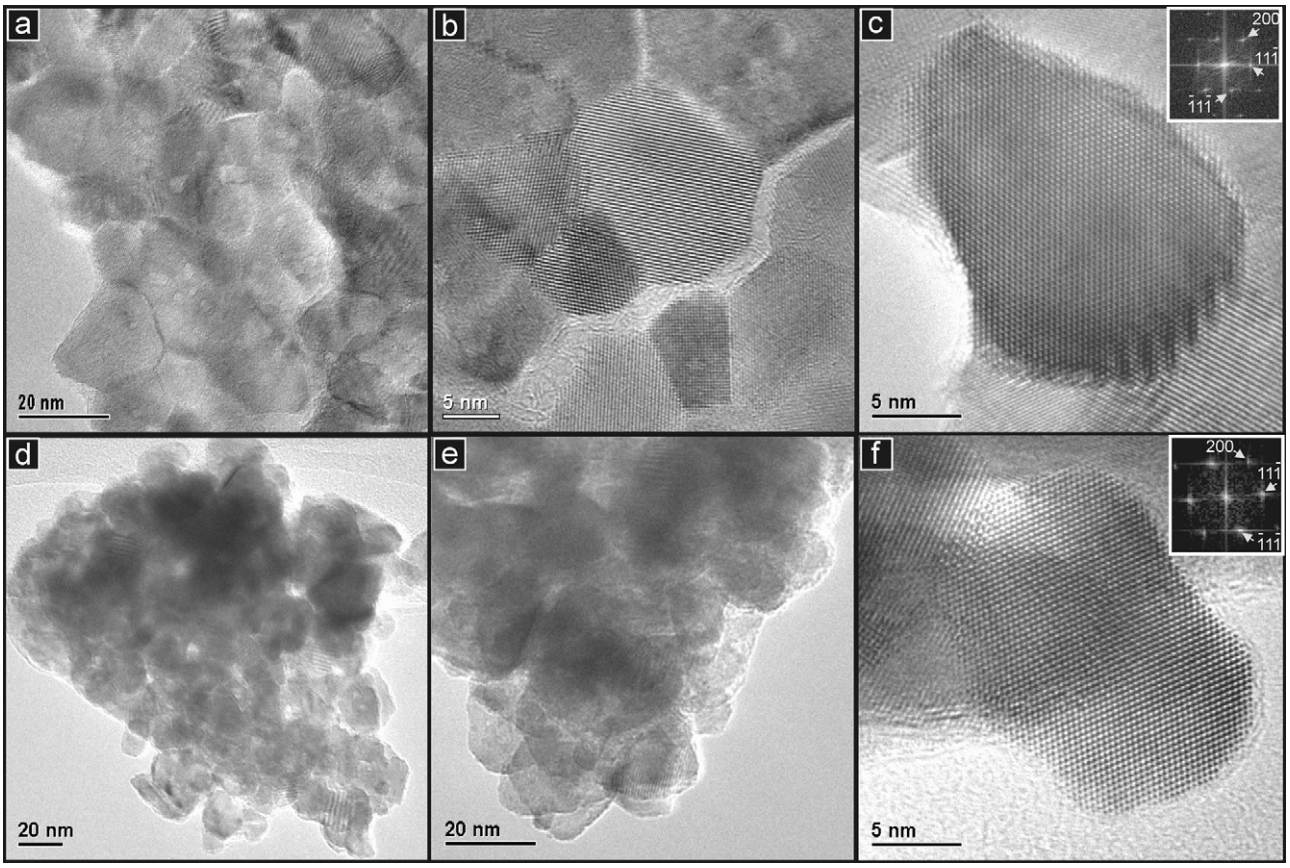

Fig. 2. TEM images at increasing magnifications of 5 wt% Pd/GDC10 samples prepared using: (a–c) cation complexation method and (d–f) incipient wetness impregnation method. The sheet-like structures with largely interlocking crystals of the 5 wt% Pd/GDC10-CC are seen in (a and b) while more three-dimensional agglomerates of particles are seen for the 5 wt% Pd/GDC10-WI in (d and e). For both samples the internal crystal structure is viewed (c and f) and gives digital diffraction patterns consistent with the cubic Fluorite structure viewed along the [0 1 1] zone axis (DDPs inset).

from the XRD results (presented below) suggests that PdO may be present within these agglomerations, or even as inclusions within the GDC10 material, making it visible to chemical analysis by EDS but where it would be difficult to distinguish individual PdO particles by use of the DDPs.

To further investigate the distribution of Pd in these samples, TEM images and corresponding elemental distribution maps for Ce, Gd, O and Pd were obtained and typical examples are presented in Fig. 4 for the CC samples and in Fig. 5 for the WI samples. Firstly, in all samples studied, Ce, Gd and O were coincident, indicating that all samples contained nanoparticulate GDC of uniform composition. There appeared to be no segregation of CeO_2 or Gd_2O_3 particles. Turning to the Pd distributions, in the 1 wt% Pd/GDC10-CC sample, the Pd appeared to be coincident with the Ce. That is, where there was Ce there was also Pd in the same apparent concentration ratio. In addition to this, however, small Pd-rich (most probably PdO) particles were also observed. A typical example is given in Fig. 4a. These were common in the 1 wt% Pd/GDC10-CC sample but less common in the 5 wt% Pd/GDC10-CC sample. The latter tended to show only the uniform distribution of Pd with Ce described above, as shown in Fig. 4b. These results suggest that the CC samples contain a uniform distribution of Pd over the GDC support in the form of small Pd-rich particles (too small to be resolved in the EDS maps) but that in addition to this there were larger Pd-rich particles (typically 20–40 nm), especially in the 1 wt% sample. The elemental maps for the WI samples were significantly different in that far fewer Pd-rich particles were resolved, the relationship between Pd and Ce concentrations was variable and the Pd was often present in patches and absent in other areas. This was the case for both the 1 and 5 wt% Pd/GDC10-WI samples, as shown in Fig. 5a and b, respectively. This suggests that the Pd-rich particles in both the WI samples were very small, since they were not resolved in the EDS maps, but that they were not uniformly distributed over the GDC support.

Table 1
Crystallite average size (D_{XRD}), specific surface area (SSA) and calculated primary particle size (d_{BET}) for Pd/GDC10 catalyst prepared by cation complexation (CC) and incipient wetness impregnation (WI).

Sample	D_{XRD} (nm)	SSA ($m^2\,g^{-1}$)	d_{BET} (nm)	d_{BET}/D_{XRD}
1 wt% Pd/GDC10-CC	21.6	33.6	25.1	1.2
1 wt% Pd/GDC10-WI	26.3	37.1	22.7	0.9
5 wt% Pd/GDC10-CC	21.5	46.7	19.7	0.9
5 wt% Pd/GDC10-WI	20.9	40.7	22.1	1.1

In Fig. 6, all XRD patterns exhibited resolvable peaks but with relatively severe line broadening. This broadening was ascribable to the presence of small crystallites. All samples exhibited an average crystallite size ranging from 21 nm to 26 nm. In Table 1, average crystallite size (D_{XRD}), SSA and calculated primary particle size (d_{BET}) for the Pd/GDC10 catalysts prepared by CC and WI are summarised. All samples exhibited values of SSA between 36.6 $m^2\,g^{-1}$ and 46.7 $m^2\,g^{-1}$. The lowest values of SSA were obtained for the 1 wt% Pd/GDC10 nanopowders. The d_{BET}/D_{XRD} ratio in all samples was close to unity, indicating that the crystallites exhibited a very low degree of agglomeration.

No diffraction peaks corresponding to Pd or PdO were observed in the XRD patterns of the 1 wt% Pd/GDC10-CC and -WI samples (Fig. 6a). Even a slow scan in the regions of the Pd (1 1 1) and

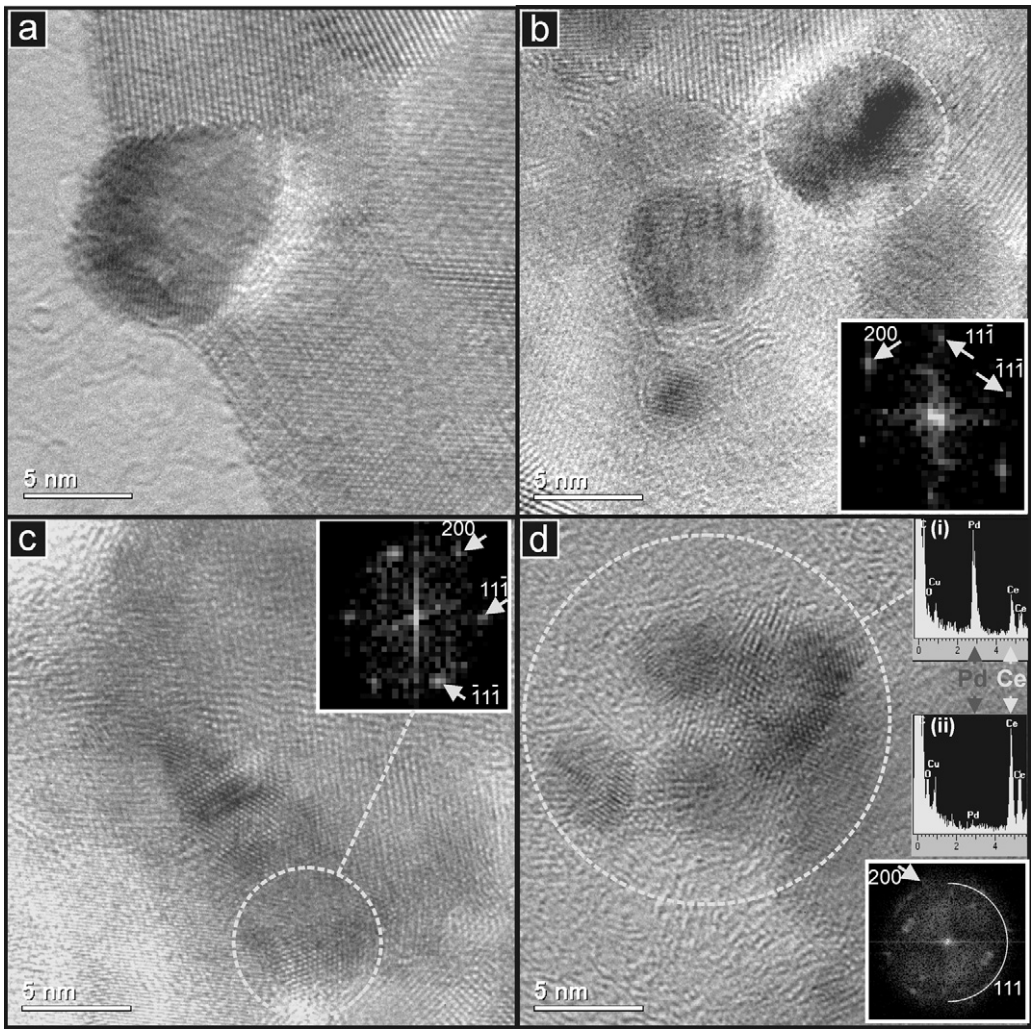

Fig. 3. TEM images of 5 wt% Pd/GDC10-CC: (a) a single Pd particle on the oxide support with some crystal planes evident; (b) a number of supported Pd particles viewed top-down. The particle circled gives a DDP consistent with the cubic structure expected for metallic Pd viewed along the [0 1 1] zone axis (DDP inset). TEM images of 5 wt% Pd/GDC10-WI: (c) Pd particles viewed top-down on the oxide support, one of which gives a DDP consistent with the cubic structure expected for metallic Pd viewed along the [0 1 1] zone axis (DDP inset); (d) a number of Pd particles on the oxide support viewed in profile (with holey carbon film below). EDS of the area circled (i) and of the support only (ii) confirm the Pd content of the particles and the DDP (inset) of the same region gives spots consistent with the 1 1 1 and 2 0 0 planes of the cubic structure expected for metallic Pd.

PdO (1 1 1) peaks did not show any indication of Pd metal or PdO. However, this is not conclusive because of the limitations of the XRD technique for detecting small amounts of minority phases. On the contrary, in samples with 5 wt% Pd (Fig. 6b), it is possible to observe the characteristic diffraction peaks, corresponding to the (1 1 1) and (2 0 0) reflections of PdO.

Synchrotron HT-XRD patterns at 500 °C in 5% H_2/He (red line) and synthetic air (black line) are given in Fig. 7. The XRD data were recorded first under reducing conditions, the atmosphere was changed to synthetic air and, after 10 min, a second XRD pattern was collected. Under reducing conditions, the main peak of metallic Pd is clearly observed in all samples. However, samples prepared by cation complexation exhibited the sharpest peaks, indicating that the crystallites of Pd in 1 and 5 wt% Pd/GDC10-CC were larger than in the same compositions prepared by WI. On the other hand, under oxidizing conditions at 500 °C, the main peaks of PdO alone were observed in all four samples. Clearly, the metallic Pd was re-oxidised. These results indicate that, at this temperature and in these samples, palladium changes easily from Pd(0) under reducing conditions to Pd(II) under oxidizing conditions.

Fig. 8a and b shows the normalised Pd L_3-edge XANES spectra obtained for the nanostructured 1 wt% and 5 wt% Pd/GDC10 samples, respectively, with the corresponding spectrum of Pd metal as a reference. Two sets of nanostructured Pd/GDC10 samples were studied: "fresh" (without any treatment) and "reduced" (reduction treatment performed in 7% H_2/N_2 at 450 °C for 1 h). Clearly, a large difference is observed between the spectra of fresh Pd/GDC10 catalysts and that of the Pd foil reference. A noticeable shift to higher energies is observed at both absorption edges for the Pd/GDC10 catalysts with respect to the foil. The fresh Pd/GDC10 spectra exhibit a large white line peak, which can be assigned to the electronic transition from Pd $2p_{3/2}$ to the unoccupied 4d states [27]. The L_3-absorption edge for Pd metal is at 3173.0 eV, while the Pd/GDC10 sample exhibited a higher value of 3174.6 eV, indicating that the Pd was in the Pd(II) oxidation state. The reduction treatment seems to have affected the oxidation state of the Pd since, in the reduced Pd/GDC10 samples, the L_3-absorption edge for Pd was observed at 3173.4 eV, indicating that the Pd was in its metallic form. These results are in good agreement with those obtained by XRD. However, small differences were observed between the spectra of the Pd foil and of the reduced Pd/GDC10. These may have been caused by the presence of a small amount of Pd(II) in the reduced catalyst samples, probably as PdO cores embedded within larger metallic Pd shells. That is, some of the larger PdO particles may only have been

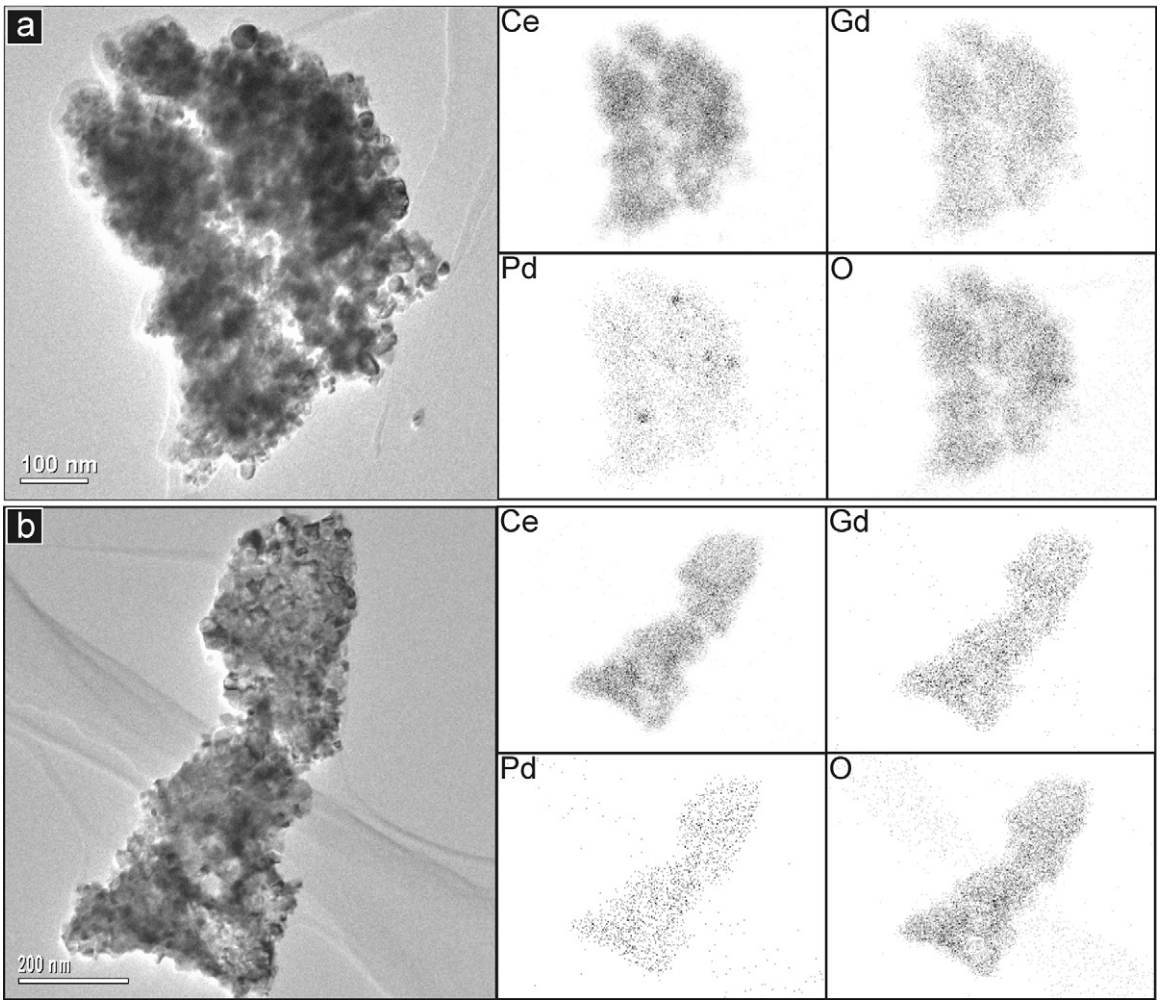

Fig. 4. TEM images and corresponding EDS distribution maps of elements as indicated for (a) 1 wt% Pd/GDC10-CC and (b) 5 wt% Pd/GDC10-CC. Element maps are rotated slightly with respect to the TEM image because of the EDS detector geometry.

partly reduced. This is a well-known effect since once the surface of the particle has been reduced, the H_2 gas must diffuse through the Pd to reduce the particle interior.

In order to determine the fraction of Ce present as Ce^{3+} in the samples, data analysis was conducted by least-squares fitting four Gaussian profiles and one arctangent function to the Ce L_3-edge XANES experimental data in the range between 5710 and 5750 eV. The assignment of the four peaks in this region is discussed below. The Ce L_3-edge is frequently used as a "fingerprint" to characterise the electronic properties of ceria-based materials. However, the electronic transitions which give rise to these XANES features are complex and not fully understood. In pure CeO_2, the Ce L_3-edge exhibits two clear peaks frequently labelled A and B. Peak A is a Ce^{4+} peak with the final state of $2p4f^0 5d^1$, which denotes that an electron is excited from the Ce 2p shell to its 5d shell, with no electron in the 4f shell. Peak B is also a Ce^{4+} peak, with the final state of $2p4f^1 5d^1 \underline{v}$, which denotes that, in addition to an electron excited from the Ce 2p shell to the 5d shell, another electron is also excited from the valence band (O 2p shell) to the Ce 4f shell, leaving a hole ($\underline{v}$) in the valence band. Some authors refer to Peak C as a Ce^{3+} peak [28]. An additional small peak (D) is present at pre-edge and likely arises from transitions to the bottom of the conduction band. In Fig. S2 (Supporting Data) it can be seen that the absorption edge, in all samples, moved to lower energy values as the temperature increased. This indicates that the Ce^{3+} content of the samples increased with increasing reduction temperature.

In Fig. 9, the Ce L_3-edge XANES spectra of the 5 wt% Pd/GDC10-CC sample under reducing conditions (5%H_2/He, 20 mL min^{-1}) at room temperature and at 600 °C and their corresponding fits are shown. The area of peak C clearly increased and that of the white line clearly decreased on going to the higher temperature. The increase in the area of peak C indicates that, under these reducing conditions, the amount of Ce present as Ce^{3+} at high temperature is larger than in the same sample at room temperature.

The ratio between the area of peak C (associated with Ce^{3+}) and the sum of the areas of peaks A, B and C (A and B are associated with Ce^{4+}) gives direct information about the fraction of Ce present as Ce^{3+}. In Fig. 10, this fraction is plotted for all samples (and a nanoceria reference material) during exposure to a flow of 5% H_2/He and over a range of temperatures from room temperature to 600 °C during an in situ TPR experiment. Ease of reduction of Ce^{4+} is seen to increase in the order: CeO_2 < GDC10 < 1 wt% Pd/GDC10-WI < 5 wt% Pd/GDC10-WI < 1 wt% Pd/GDC10-CC < 5 wt% Pd/GDC10-CC. This figure clearly shows the increase in reducibility on doping pure ceria with Gd (so introducing oxygen ion vacancies) as well as the significant increase in reducibility caused by the incorporation of Pd in the CC and WI samples. Although some nanoparticles of Pd were detected by TEM (Fig. 3), the XRD results imply that almost all Pd is present as PdO initially (Fig. 6). In Fig. 10, two mechanisms for reduction of the Ce are possible: (1) direct adsorption of H_2 on the oxide, followed by reaction and release of water and (2) reduction of PdO to Pd with subsequent adsorption of H_2 on the Pd

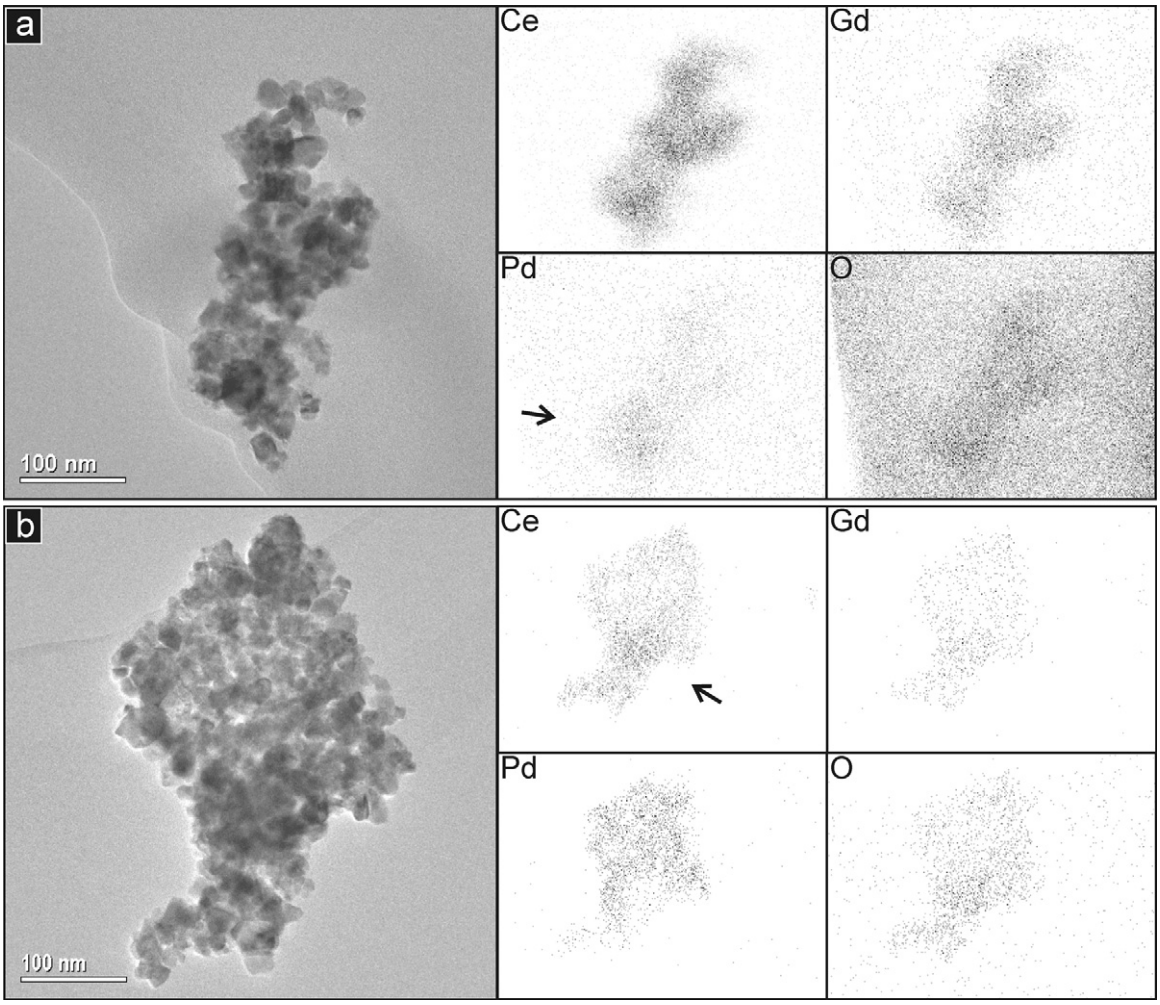

Fig. 5. TEM images and corresponding EDS distribution maps of elements as indicated for (a) 1 wt% Pd/GDC10-WI and (b) 5 wt% Pd/GDC10-WI. Arrows indicate regions where there is strong mismatch between Pd and Ce concentrations. Element maps are rotated slightly with respect to the TEM image because of the EDS detector geometry.

and spillover of H species onto the oxide surface, where these can reduce the oxide and again form water. Evidence of facile reduction of PdO to Pd is given in the synchrotron XRD data in Fig. 7 and spillover of hydrogen from Pd nanoparticles is known to occur easily, even at low temperatures [29–31]. Therefore, reduction via spillover from the Pd nanoparticles is likely to dominate over direct reduction of the oxide. This explains the increase in reducibility on going from GDC to Pd/GDC materials. The differences between the Pd/GDC samples can be explained by referring to the distribution of Pd given in the EDS maps in Figs. 4 and 5. For effective reduction of the Ce, Pd must be in intimate contact with the GDC10 support. Pd nanoparticles must be at a sufficiently high concentration over the whole surface of the GDC to allow spillover to all parts of the support and so to enable the most effective reduction. The EDS maps of the CC samples show a close relationship between Ce and Pd distribution, even though there were also many relatively large particles (20–40 nm), especially in the 1 wt% Pd sample. In both WI samples, the Pd distribution was patchy, there being regions of the GDC where there was very little Pd. This difference explains why the CC samples were more easily reduced than the WI samples. Increasing Pd loading in both cases increased Pd concentration and would be expected therefore to increase ease of reduction, as is the case. For the CC samples, the increase in reducibility is large, because of the favourable Pd distribution and also the decrease in the number of larger particles on going from 1 wt% Pd/GDC10-CC to 5 wt% Pd/GDC10-CC. For the WI samples, the improvement in reducibility is much smaller. From the EDS maps, this can be explained because the Pd is still patchily distributed in the 5 wt% Pd/GDC10-WI sample, even though the amount of Pd present had increased.

3.2. Catalytic test for CH_4 combustion

In order to obtain an indication of their catalytic activity, several tests were performed on the Pd/GDC10 materials, as explained in Section 1. For comparison, similar tests were performed on nanopowders of CeO_2, GDC10 and without a catalyst (blank). In Fig. 11, CH_4 conversion versus temperature for the different catalyst samples is plotted. The temperature at which 50% of CH_4 conversion was reached (T_{50}) was used as an index of catalytic activity. T_{50} values were estimated from the experimental curves and are given in Table 2. The blank test exhibited the highest value of T_{50} (883 °C). The 5 wt% Pd/GDC10 samples (CC and WI) exhibited very similar behaviour, gave the lowest values of T_{50} and, therefore, appeared to be the most active catalysts under these conditions. The high Pd content seems to have been responsible for the enhanced catalytic activity of the 5 wt% Pd/GDC10 catalysts. There was a marked improvement in T_{50} going from pure GDC to 1 wt% Pd/GDC10-CC, and an even greater one on then going to 5 wt% Pd/GDC-CC. Although the two 5 wt% catalysts behaved very similarly, the 1 wt% Pd/GDC10-CC catalyst gave a significantly lower value of T_{50} than the corresponding sample prepared by WI.

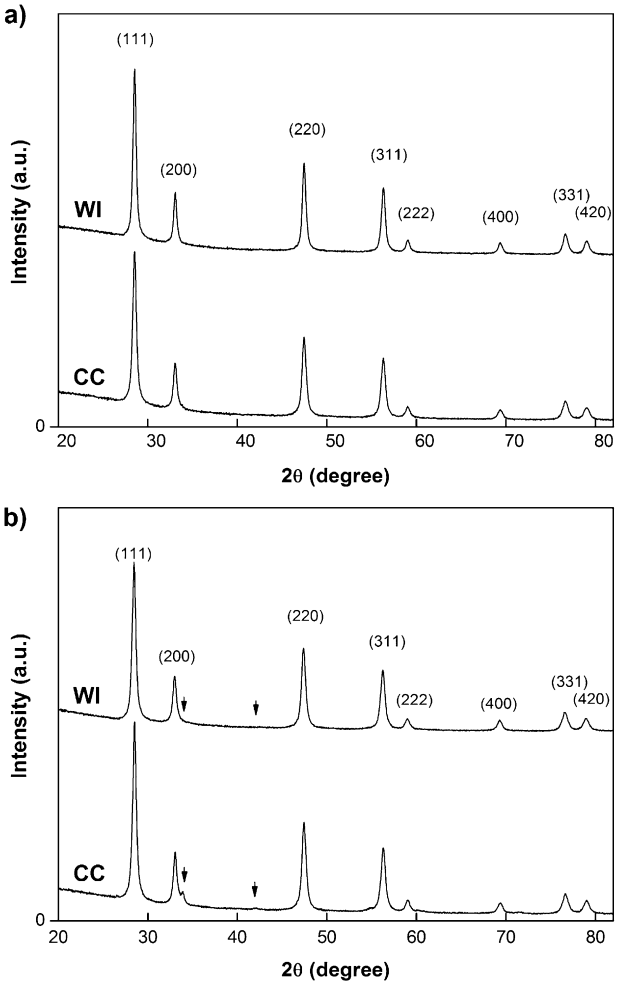

Fig. 6. XRD patterns of (a) 1 wt% Pd/GDC10 prepared by CC (lower) and WI (upper) methods, and (b) 5 wt% Pd/GDC10 prepared by CC (lower) and WI (upper) methods. Black arrows indicate main PdO peaks.

Table 2
Values of temperature at which 50% of CH_4 conversion was reached (T_{50}), estimated from the experimental curves.

Sample	T_{50} (°C)
Blank	883
CeO_2	680
GDC10	640
1 wt% Pd/GDC10-CC	427
1 wt% Pd/GDC10-WI	515
5 wt% Pd/GDC10-CC	373
5 wt% Pd/GDC10-WI	367

The overall proposed explanation for this behaviour is as follows. Ceria-based mixed oxide materials are known to act as oxygen storage materials, or oxygen buffers, in oxidation reactions because of the accessible Ce^{3+}/Ce^{4+} redox couple. Reduction of Ce^{4+} to Ce^{3+} is accompanied by loss of oxygen from the oxide. Ceria-based materials are able to follow the Mars Van Krevelen mechanism in which the catalyst acts as the oxygen donor towards the reactant and this oxygen is replenished from the oxygen present in the gas phase and which thus acts as an indirect reactant, so keeping the catalyst in its oxidised, active form [32]. In the present work, the catalytic tests were carried out in excess oxygen, so this mechanism was favoured.

In pure GDC, Gd^{3+} ions introduce extrinsic oxygen vacancies, which in turn diminish the Ce^{3+} content in the material from a simple equilibrium point of view [10]. The GDC10 then shows a higher Ce^{4+} content than pure ceria (under the same external conditions), and, it is proposed that, as a consequence, it displays higher catalytic activity. The higher oxygen vacancy concentration would also tend to allow faster loss and uptake of oxygen from the gas phase, so improving the redox kinetics. T_{50} data for pure ceria and pure GDC10 showed precisely this behaviour in Fig. 11 (680 °C vs. 640 °C, respectively).

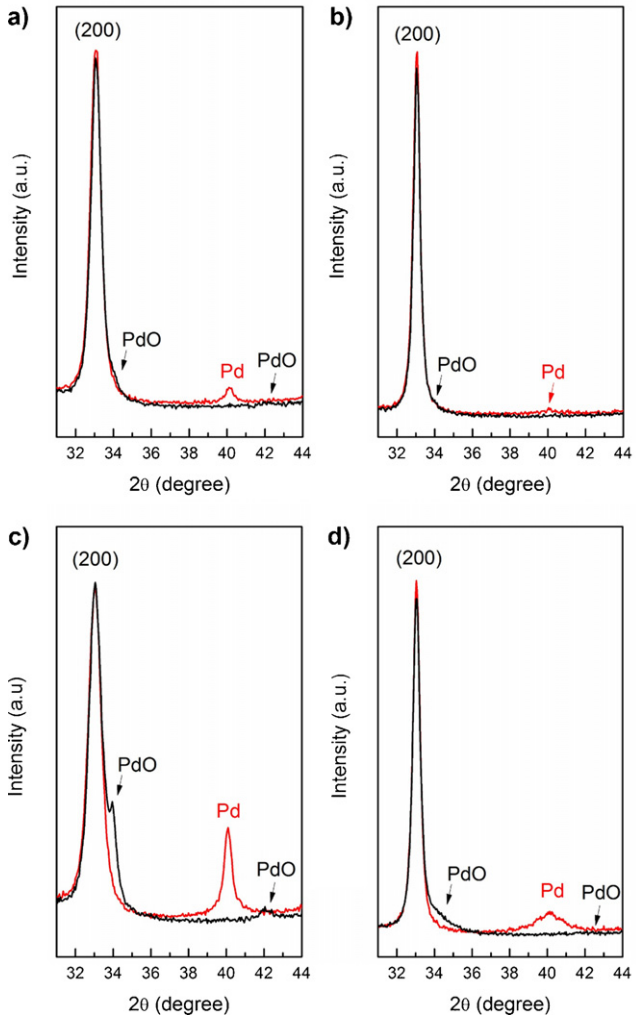

Fig. 7. Synchrotron HT-XRD patterns of (a) 1 wt% Pd/GDC10-CC, (b) 1 wt% Pd/GDC10-WI, (c) 5 wt% Pd/GDC10-CC and (d) 5 wt% Pd/GDC10-WI samples at 500 °C under reducing (red line) and oxidizing (black line) conditions. (For interpretation of the references to colour in this figure legend, the reader is referred to the web version of this article.)

In Pd-containing materials, the exact catalytic mechanism for hydrocarbon oxidation is not fully understood, and neither are the species that are involved. Nevertheless, there is a general consensus that the active phase is probably PdO or an equivalent intermediate, but that metallic Pd shows worse or no catalytic activity at all [33–35]. There is also evidence for the enhancement effect conferred by ceria-related materials on the PdO active phase and hence on the catalytic activity [36,37]. Even in the case of catalytic tests using unsupported Pd, it was shown that the active phase for hydrocarbon oxidation is PdO and not metallic Pd [38].

In our case, XRD and HRTEM results indicate that, certainly at the higher Pd doping level (5 wt%), Pd is not incorporated into the GDC10 lattice, but rather is present as segregated PdO and Pd phases. XANES spectra at the Pd-L_3 edge also showed that at an equal Pd loading, reductive treatment caused the Pd to change from

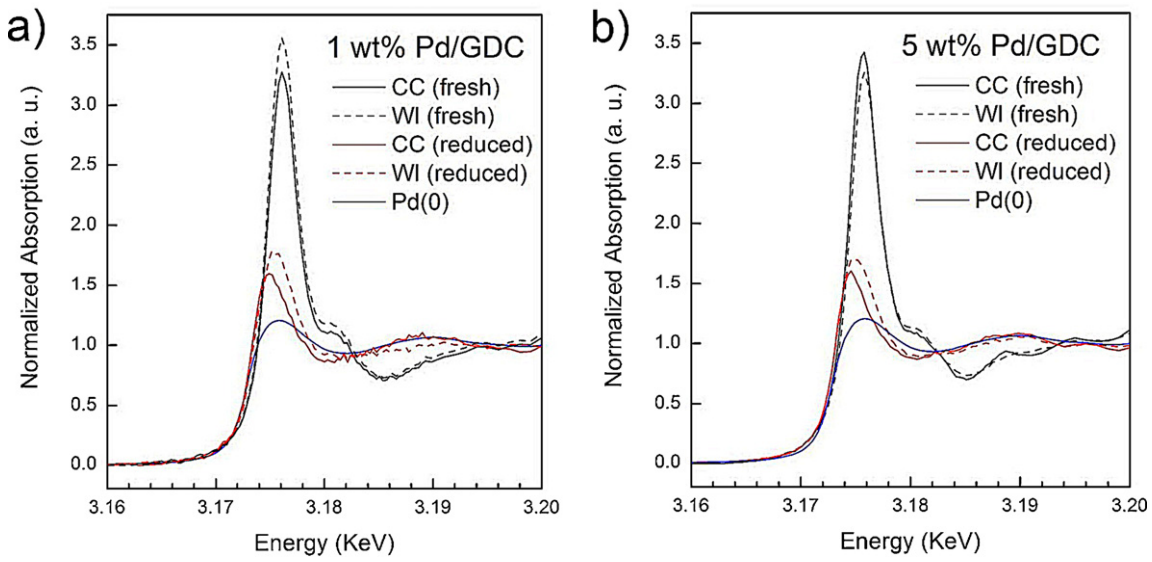

Fig. 8. Normalised Pd L_3-edge XANES absorption spectra for (a) 1 wt% Pd/GDC10 and (b) 5 wt% Pd/GDC10 at room temperature prepared by the methods indicated. Pd metal foil is included for comparison (blue line). (For interpretation of the references to colour in this figure legend, the reader is referred to the web version of this article.)

being mainly present as PdO to being mostly present as metallic Pd. This strongly suggests that the Pd is to be found mainly outside the GDC10 lattice. However, here GDC not only acts as a support for Pd/PdO, but also plays a major role (albeit somewhat indirect) in the catalytic activity, since it serves as an oxygen source for the Pd/PdO hysteresis, allowing the active PdO phase to be regenerated (something favoured by the oxidised state of the GDC10 in the oxygen-rich gas environment in the catalytic tests and by the good oxygen ion conductivity of the GDC10). Additional catalytic tests (not included here) were made on Pd/GDC10 samples that had been pre-reduced in hydrogen. These displayed T_{50} results virtually identical to those shown by their original unreduced counterparts. This indicates that the active PdO phase was regenerated from the metallic Pd in the reduced samples upon treatment of these with the oxygen-rich feed in the catalytic tests.

In summary, the proposed explanation is that the GDC10 constantly provided oxygen to the active catalytic sites and that the GDC10 itself is constantly reoxidised (and hence kept in its active form) by the oxygen from the gas feedstock.

The results presented in Fig. 11 show that the 1 wt% Pd/GDC10-WI sample had a higher T_{50} value than the 1 wt% Pd/GDC10-CC sample which had the same Pd loading. This can be explained by considering the distribution of Pd resulting from the two preparation methods. EDS maps in Figs. 4 and 5 showed that the WI method gave rise to a more patchy distribution of Pd than the CC method. In the latter, the Ce and Pd concentrations were very closely related,

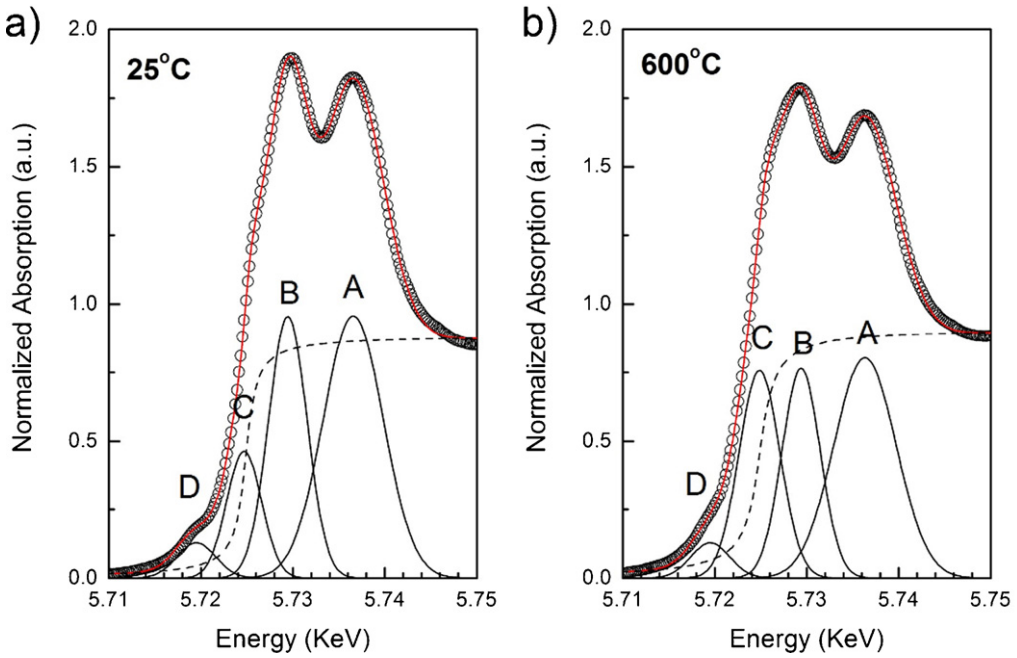

Fig. 9. Normalised Ce L_3-edge XANES absorption spectra for 5 wt% Pd/GDC10-CC (a) at room temperature and (b) at 600 °C under reducing conditions, showing the experimental data (empty circles), four Gaussian peaks (A–D), and one arctangent function (dotted line) obtained by least-squares fitting (continuous black lines) and the sum of all five functions (continuous red line). (For interpretation of the references to colour in this figure legend, the reader is referred to the web version of this article.)

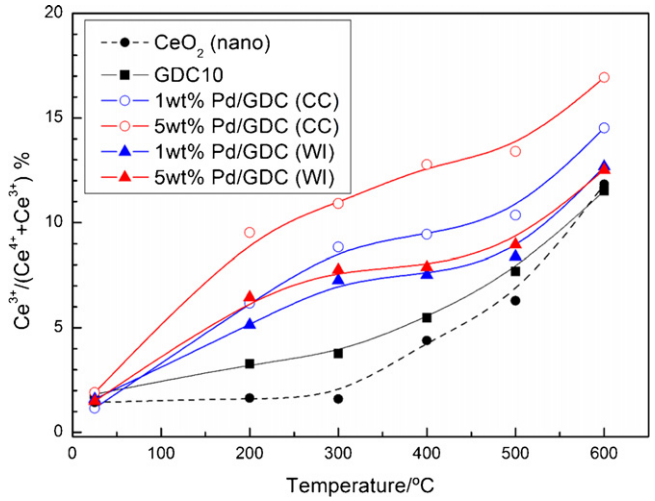

Fig. 10. Fraction of Ce present as Ce^{3+} in nanostructured GDC10, 1 wt% Pd/GDC10-CC, 1 wt% Pd/GDC10-WI, 5 wt% Pd/GDC10-CC and 5 wt% Pd/GDC10-WI under reducing conditions as a function of temperature. Micropowders and nanopowders of CeO_2 are included for comparison.

across the samples, thus providing a more effective distribution of the active PdO/GDC10 sites.

The fact that both 5 wt% Pd/GDC10 samples show essentially the same T_{50} values does not necessarily contradict the points proposed in the previous paragraph. The EDS maps in Figs. 4 and 5 show that the Pd distribution in the catalysts prepared by both the CC and WI methods is not adversely affected by increasing the Pd loading and, indeed, the catalysis test results show that there was an increase in catalytic activity in both cases on increasing Pd loading from 1 wt% to 5 wt%. The fact that the activities of the 5 wt% catalysts prepared by the two different methods are more similar than in the case of the 1 wt% loadings can be explained as a saturation effect. A Pd loading will be reached at which there are so many PdO particles that the processes they catalyse will be fast enough to cease to be rate limiting. Another process, for example, reoxidation of the GDC10, will then control the rate of reaction. It is proposed that this point had been reached for both CC and WI catalysts at a loading of 5 wt%, thus explaining the similar catalytic behaviour of these two samples.

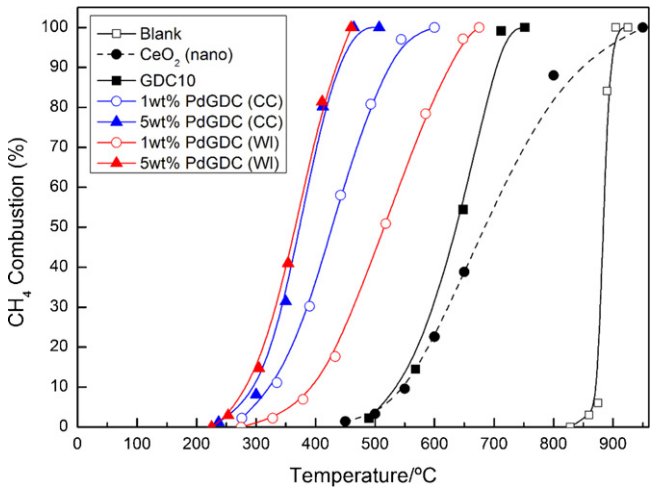

Fig. 11. Catalytic results of CH_4 combustion for nanostructured 1 wt% Pd/GDC10-CC, 1 wt% Pd/GDC10-WI, 5 wt% Pd/GDC10-CC and 5 wt% Pd/GDC10-WI samples as a function of temperature. Nanopowders of CeO_2, GDC10 and non-catalytic sample (blank) are included for comparison.

Finally, it should be noted that the catalytic activity that stems from the PdO/GDC10 sites acts in parallel with the catalytic activity expected from any ceria-based material, due to the presence of the Ce^{3+}/Ce^{4+} redox couple.

4. Conclusions

In the present work, 1 wt% and 5 wt% Pd/GDC10 nanopowders were prepared by two different methods: (a) CC and (b) incipient WI of an aqueous Pd^{2+} solution onto GDC10 nanopowders. All samples were characterised by XRD, XANES, HRTEM and EDS.

Pd L_3-edge XANES absorption experiments confirmed that Pd is present mainly as PdO in these samples and that the Pd is easily reduced to its metallic form on exposure to hydrogen at elevated temperatures.

The addition of Pd to the GDC10 nanopowders increased the reducibility of the Ce in the mixed oxide. This was demonstrated by analysis of in situ XANES spectra obtained under reducing conditions.

Catalysts with the higher Pd loading (5 wt%) exhibited the best performance for CH_4 combustion. The influence of preparation method was evident for catalysts with 1 wt% Pd, CC resulting in more active catalysts than the WI method. This was explained as a consequence of differences in Pd distribution as observed in EDS element maps.

These findings open up an interesting avenue for future work in this area, and indicate a promising possible application for this particular system.

Acknowledgments

This work has been supported by: the Brazilian Synchrotron Light Laboratory (LNLS, Brazil), under proposals D04A-SXS-11749, D04B-XAFS1-11748 and D12A-XRD1-13563; the Agencia Nacional de Promoción Científica y Tecnológica (Argentina, PICT No. 01152) and PIDDEF No. 0011/11 CITEDEF. TEM and EDS were performed by RTB at the Electron Microscopy Facility, University of St Andrews. Special thanks to M. Cabezas and Dr. S. Larrondo for useful discussions regarding the catalytic tests. Dr. R.O. Fuentes is a member of CIC-CONICET, Argentina.

Appendix A. Supplementary data

Supplementary data associated with this article can be found, in the online version, at http://dx.doi.org/10.1016/j.apcatb.2013.02.008.

References

[1] R. Di Monte, J. Kaspar, Topics in Catalysis 28 (2004) 47–57.
[2] S.D. Park, J.M. Vohs, R.J. Gorte, Nature 404 (2000) 265–267.
[3] S.M. Haile, Materials Today 6 (2003) 24–29.
[4] B.H.C. Steele, Nature 400 (1999) 619–621.
[5] B.H.C. Steele, Solid State Ionics 129 (2000) 95–110.
[6] J.A. Kilner, Solid State Ionics 123 (2000) 13–23.
[7] J. Kaspar, P. Fornasiero, in: A. Trovarelli (Ed.), Catalysis by Ceria and Related Materials, Imperial College Press, London, 2002, pp. 217–236.
[8] A.A. Yaremchenko, A.A. Valente, V.V. Kharton, I.A. Bashmakov, J. Rocha, F.M.B. Marques, Catalysis Communications 4 (2003) 477–483.
[9] S.P. Jiang, X.J. Chen, S.H. Chan, J.T. Kwok, Journal of the Electrochemical Society 153 (5) (2006) A850–A856.
[10] U. Hennings, R. Reimert, Applied Catalysis B 70 (2007) 498–508.
[11] R.O. Fuentes, F.F. Muñoz, L.M. Acuña, A.G. Leyva, R.T. Baker, Journal of Materials Chemistry 18 (2008) 5689–5795.
[12] F.F. Muñoz, A.G. Leyva, R.T. Baker, R.O. Fuentes, International Journal of Hydrogen Energy 37 (2012) 14854–14863.
[13] R.T. Baker, I.S. Metcalfe, P.H. Middleton, B.C.H. Steele, Solid State Ionics 72 (1994) 328–333.
[14] R.T. Baker, I.S. Metcalfe, Applied Catalysis A 126 (1995) 297–317.
[15] R.T. Baker, I.S. Metcalfe, Applied Catalysis A 126 (1995) 319–332.

[16] S. Tao, J.T.S. Irvine, S.M. Plint, Journal of Physical Chemistry B 110 (2006) 21771–21776.
[17] R.O. Fuentes, R.T. Baker, Journal of Physical Chemistry C 113 (2009) 914–924.
[18] S. Song, R.O. Fuentes, R.T. Baker, Journal of Materials Chemistry 20 (2010) 9760–9769.
[19] J. Kearney, J.C. Hernández-Reta, R.T. Baker, Catalysis Today (2012) 139–147.
[20] P. Bera, K.C. Patil, V. Jayaram, G.N. Subbanna, M.S. Hegde, Journal of Catalysis 196 (2000) 293–301.
[21] K.R. Priolkar, P. Bera, P.R. Sarode, M.S. Hegde, S. Emura, R. Kumashiro, N.P. Lalla, Chemistry of Materials 14 (2002) 2120–2128.
[22] F.F. Muñoz, M.D. Cabezas, L.M. Acuña, A.G. Leyva, R.T. Baker, R.O. Fuentes, Journal of Physical Chemistry C 115 (2011) 19687–19696.
[23] R.O. Fuentes, R.T. Baker, International Journal of Hydrogen Energy 33 (2008) 3080–3084.
[24] R.O. Fuentes, R.T. Baker, Journal of Power Sources 186 (2) (2009) 268–277.
[25] H. Klug, L. Alexander, X-ray Diffraction Procedures for Polycrystalline and Amorphous Materials, John Wiley, New York, 1974, p. 618.
[26] T.J. Ressler, Synchrotron Radiation 5 (1998) 118–122.
[27] K. Shimizu, R. Maruyama, S. Komai, T. Kodama, Y. Kitayama, Journal of Catalysis 227 (2004) 202–209.
[28] F. Zhang, P. Wang, J. Koberstein, S. Khalid, S.-W. Chan, Surface Science 563 (2004) 74–82.
[29] J.M. Gatica, R.T. Baker, P. Fornasiero, S. Bernal, J. Kašpar, Journal of Physical Chemistry B 105 (2001) 1191–1198.
[30] A. Norman, V. Perrichon, Physical Chemistry Chemical Physics 5 (2003) 3557–3564.
[31] F.C. Gennari, A. Carbajal Ramos, A. Condó, T. Montini, S. Bengió, A. Cortesi, J.J. Andrade Gamboa, P. Fornasiero, Applied Catalysis A 398 (2011) 123–133.
[32] J.L.G. Fierro, Metal Oxides Chemistry, CRC Press, Boca Raton, Florida, USA, 2006, p. 217 (Chapter 8).
[33] S. Colussi, A. Trovarelli, E. Vesselli, A. Baraldic, G. Comelli, G. Groppi, J. Llorca, Applied Catalysis A 390 (2010) 1–10.
[34] S. Colussi, A. Trovarelli, G. Groppi, J. Llorca, Catalysis Communications 8 (2007) 1263–1266.
[35] A. Hellman, A. Resta, N.M. Martin, J. Gustafson, A. Trinchero, P.A. Carlsson, O. Balmes, R. Felici, R. van Rijn, J.W.M. Frenken, J.N. Andersen, E. Lundgren, H. Grönbeck, The Journal of Physical Chemistry Letters 3 (2012) 678–682.
[36] L.M.T. Simplício, S.T. Brandão, D. Domingos, F. Bozon-Verduraz, E.A. Sales, Applied Catalysis A 360 (2009) 2–7.
[37] L. Meng, J.-J. Lin, Z.-Y. Pu, L.-F. Luo, A.-P. Jia, W.-X. Huang, M.-F. Luo, J.-Q. Lu, Applied Catalysis B 119–120 (2012) 117–122.
[38] B.G. Hoflund, H.A.E. Hagelin, J.F. Weaver, G.N. Salaita, Applied Surface Science 205 (2003) 102–112.